Experimental verification of two-dimensional spatial harmonic analysis at oblique light incidence

Zhengtong Liu, Kuo-Ping Chen, Xingjie Ni, Vladimir P. Drachev, Vladimir M. Shalaev, and Alexander V. Kildishev*

School of Electrical and Computer Engineering and Birck Nanotechnology Center, Purdue University, West Lafayette, Indiana 47907, USA
**Corresponding author: a.v.kildishev@ieee.org*

Received July 28, 2010; accepted September 10, 2010;
posted September 21, 2010 (Doc. ID 132360); published November 3, 2010

We use a nanofabricated gold grating to validate two-dimensional spatial harmonic analysis (2D SHA) method, also known as Fourier modal method or rigorous coupled-wave analysis under oblique incidence. The transmittance spectra of the metal grating for incident angles of 0°–30° are obtained in both experiments and simulations at the zero diffraction order. The simulations are performed with our custom software, a fully functional web-based 2D SHA tool, which has been staged at nanoHUB.org and is free to use. The simulation results are compared to experimentally measured values, and a good fit is achieved for all incident angles. Possible reasons for experiment-simulation mismatch in actual nano-plasmonic structures are also discussed.

OCIS codes: 050.6624, 160.3918.

1. INTRODUCTION

Spatial harmonic analysis (SHA), also known as Fourier modal method or rigorous coupled-wave analysis, is a method to solve Maxwell's equations for periodic gratings. The approach dates back to the 1960s [1], when Burckhardt studied sinusoidally modulated diffraction gratings. Later this method was extended to include non-sinusoidal and complex dielectric constants modulation by Kaspar [2] and generalized by Knop [3] and Moharam and Gaylord [4,5]. A fast-converging formulation for transverse magnetic (TM) polarization was proposed in 1996 by Lalanne and Morris [6] and Granet and Guizal [7]. The mathematical foundation of this formulation was given by Li [8]. Li also provided a stable recursive matrix algorithm for thick multilayer gratings [9,10]. These formulations have been employed in our work for two-dimensional (2D) metamaterials.

Metamaterials have drawn great research interests recently due to their unique properties such as negative refractive index and potential applications such as a superlens [11]. Several metamaterial designs based on nanoscale metal structures have been realized and characterized [12–17]. However the effective properties of these metamaterials were only studied for normally incident light, whereas for a number of applications, such as a superlens, their characteristics under oblique incidence are also important. Several numerical modeling techniques, such as finite element method, finite difference time-domain method, and SHA, have been employed to study metamaterials [12,15,17,18]. Among those methods SHA is naturally suited for modeling metamaterials under oblique light incidence; hence it is the purpose of this paper to experimentally validate SHA for modeling plasmonic nanostructures. We demonstrate, for the first time to the best of our knowledge, a good agreement between experimental and SHA numerical results, obtained for a subwavelength-periodic plasmonic structure over a broad spectral range for different polarizations and incident angles. We also discuss possible reasons for experiment-simulation mismatch, such as fabrication tolerances and imperfections in nanostructured metallic elements.

This paper is arranged as follows: in Section 2 we present a brief 2D SHA formulation based on the fast-converging SHA algorithm [6,7] (details are given in the Appendix); Section 3 describes the design, fabrication, and characterization of the device; and in Section 4 we compare the experimentally measured spectra with 2D SHA simulation results and discuss the convergence of the SHA. The SHA simulations can be reproduced using the online tool PhotonicsSHA-2D [19].

2. 2D SHA FORMULATION

An N-layer single-period grating studied by 2D SHA is illustrated in Fig. 1. In each layer, the permittivity ε is modulated periodically along the y direction with a period of d and is invariant along x and z directions, and the refractive indices of the incident and output media are n_1 and n_2, respectively. In each layer Maxwell's equations can be converted into an eigenvalue equation. For transverse electric (TE) polarization the eigenvalue equation is

$$\tilde{k}_{xm}^2 \mathbf{E}_m = (\varepsilon - \tilde{\mathbf{k}}_y^2)\mathbf{E}_m, \tag{1}$$

where $\tilde{k}_{xm}$ and $\tilde{k}_y$ are the normalized wave vectors along x and y, respectively; $\mathbf{E}_m$ is the electric field magnitudes of the Fourier components; and ε is a matrix generated by

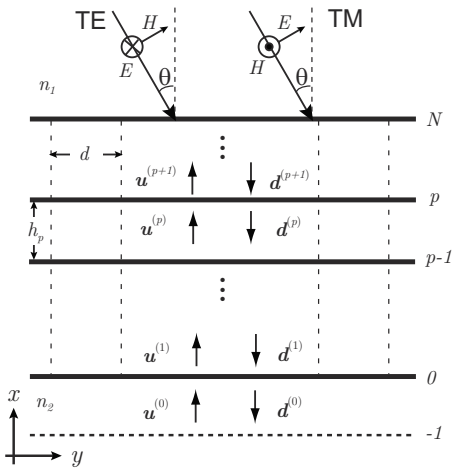

Fig. 1. Multilayer single-period grating studied in 2D SHA. The period is d. Each layer has a thickness h_p.

material permittivities. For TM polarization the eigenvalue equation is

$$\tilde{k}_{xm}^2 \mathbf{H_{zm}} = \bar{\varepsilon}^{-1}(\mathbf{I} - \tilde{\mathbf{k}}_y \varepsilon^{-1} \tilde{\mathbf{k}}_y)\mathbf{H_{zm}}, \tag{2}$$

where $\mathbf{H_{zm}}$ is the magnetic field magnitudes of the Fourier components, and $\bar{\varepsilon}$ is a matrix generated by material permittivities. We can then cascade the layers using the S-matrix method to find the final solution [9]

$$\begin{bmatrix} \mathbf{u}^{(N+1)} \\ \mathbf{d}^{(0)} \end{bmatrix} = \begin{bmatrix} \mathbf{T}_{uu}^{(N)} & \mathbf{R}_{ud}^{(N)} \\ \mathbf{R}_{du}^{(N)} & \mathbf{T}_{dd}^{(N)} \end{bmatrix} \begin{bmatrix} \mathbf{u}^{(0)} \\ \mathbf{d}^{(N+1)} \end{bmatrix}, \tag{3}$$

where $\mathbf{u}$ and $\mathbf{d}$ are magnitudes of upward and downward propagating waves, $\mathbf{T}_{uu}^{(N)}$ and $\mathbf{T}_{dd}^{(N)}$ are two transmission matrices, and $\mathbf{R}_{ud}^{(N)}$ and $\mathbf{R}_{du}^{(N)}$ are two reflection matrices. The definitions and additional details of the above equations are discussed in the Appendix.

3. DESIGN, FABRICATION, AND CHARACTERIZATION OF THE SAMPLE

The grating sample we used to verify 2D SHA modeling is illustrated in Fig. 2(a). A gold grating was fabricated with electron beam lithography on a glass substrate coated by 15 nm thick indium tin oxide (ITO) layer. The designed dimensions of the sample are listed in Table 1. First, a poly(methyl methacrylate) A4 (MicroChem Corp.) photoresist was spin-coated onto the ITO glass substrate at 3000 rpm for 60 s. Following a 90 s pre-bake of the photoresist at 180°C, an electron beam direct writing system (Vistec) was used to define the pattern with 100 kV, 1 nA, and 800 μC/cm2. Methyl isobutyl ketone: isopropanol (1:3) was used to develop the photoresist for 45 s and O2 plasma etching (Branson) at 100 W for 5 s was used for the descum process to remove residual photoresist for improved lift-off. Then electron beam evaporation was used to produce a 50 nm thick gold film with a 1 Å/s deposition rate in a 1×10^{-6} Torr vacuum chamber. After film deposition, lift-off was performed by immersion in Remover PG (MicroChem Corp.) for 6 h. A field-emission scanning electron microscope image shows the top view of the fabricated device [Fig. 2(b)]. Due to the nature of nano-

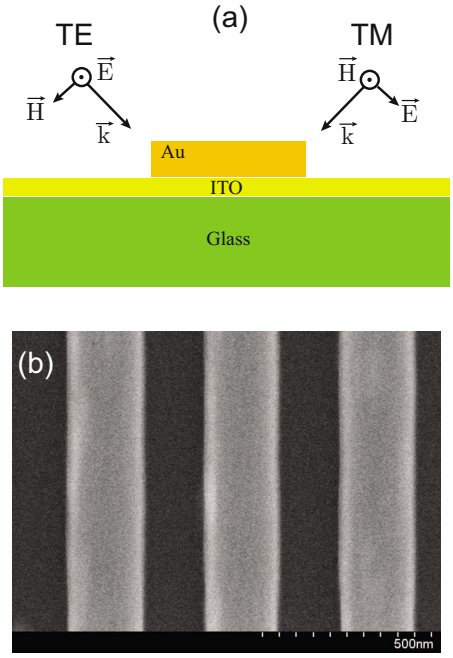

Fig. 2. (Color online) (a) Schematic of a unit cell of the structure under study; (b) SEM image of the fabricated device.

fabrication, the actual dimensions of the device could not be controlled exactly, and deviations from the designed values were inevitable. The device was then characterized using optical transmittance spectroscopy with the incident angle varying from 0° to 30°. The transmittance spectra for both TE and TM polarizations were taken in the wavelength range from 450 to 850 nm (Fig. 3).

4. 2D SHA MODELING OF THE SAMPLE

The transmittance of the device was simulated using 2D SHA with five Fourier modes for TE polarization and 15 Fourier modes for TM polarization [19]. The refractive indices of the glass substrate and the ITO film were obtained using spectroscopic ellipsometry (VASE JA Woollam Co., Inc.). The refractive index of gold was taken from [20]. Since the actual device was different from the design, we fine-tuned the dimensions, including the period, width, and thickness of the gold strips, to match the experimental spectra. It has been observed that the loss in nano-structured metal could be higher than in bulk metal, and the higher loss can be described by a loss factor [21]; therefore in our simulations a loss factor for gold was also introduced as a fitting parameter. The fitted parameters are listed in Table 1. The simulated transmittance spectra using the fitted parameters are compared to experimental spectra in Fig. 3.

Table 1. Designed and Fitted Parameters of the Sample

	Period (nm)	Thickness (nm)	Width (nm)	Loss factor
Design	400	50	200	1
Fitted	403	49	210	2.2

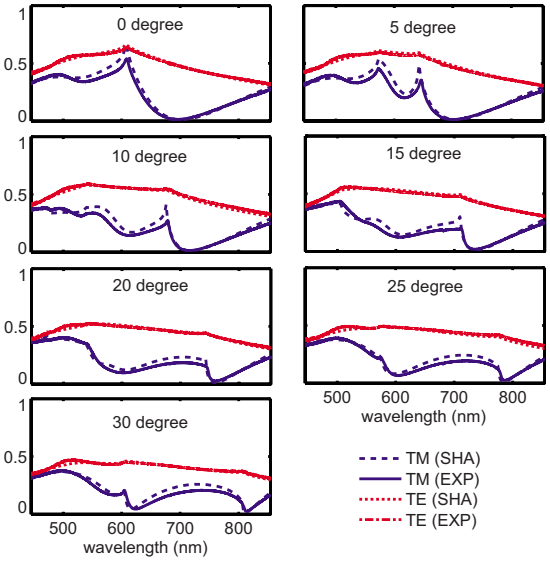

Fig. 3. (Color online) Transmittance spectra for both TE and TM polarizations at incident angles of 0°, 5°, 10°, 15°, 20°, 25°, and 30°. The experimental and SHA simulated spectra are both shown for comparison.

The spectra features in Fig. 3 were caused by a resonance in the TM polarization, such as the dip at 700 nm for 10° incidence, and by diffraction. The wavelengths at which the −1 and 1 transmission diffraction orders start can be calculated using $d(n_2+\sin\theta_i)$ and $d(n_2-\sin\theta_i)$, respectively, where d is the period, n_2 is the refractive index of the glass substrate, and θ_i is the incident angle [22]. The wavelength at which the −1 reflection diffraction order starts can be calculated by $d(1+\sin\theta_i)$. These wavelengths for different incident angles are listed in Table 2. Comparing the wavelength list in Table 2 to the spectra in Fig. 3, we see that all the diffraction features within the wavelength range we studied can be identified in the transmittance spectra, although some are stronger than others. Overall the simulated spectra matched the experimental spectra well, with all the important features reproduced, especially the plasmonic resonances originated from sub-wavelength metallic structures.

The mismatch between the experimental and numerical results is likely due to the nonuniformity of the sample: the width of the strips had small variations, the metal was deposited by electron beam evaporation and therefore grain size was not uniform, both of which can lead to spectral feature broadening but were not accounted for in the SHA simulations [21,23]. From Fig. 3 we conclude that for both polarizations and all incident angles, the 2D SHA simulations reproduced the experimental spectra with high fidelity.

Table 2. Wavelengths of Different Diffraction Orders

Incident angle (degree)	0	5	10	15	20	25	30
Transmission: −1 (nm)	613	647	683	717	750	783	814
Transmission: 1 (nm)	613	577	543	508	475	442	411
Reflection: −1 (nm)	403	438	473	507	541	573	604

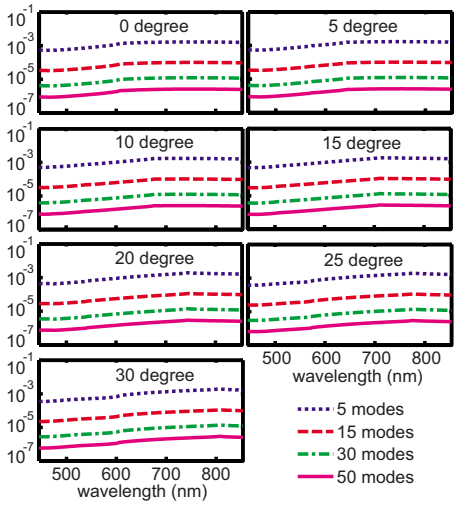

Fig. 4. (Color online) Convergence of 2D SHA for TE polarization. The difference spectra between 5, 15, 30, and 50 Fourier modes and the reference are plotted. The reference spectra are simulated using 2D SHA with 100 modes.

The convergence rate of SHA has been an important issue, especially for TM polarization [6,7]. In Fig. 4 we show the convergence of 2D SHA for TE polarization. We used spectra with 100 Fourier modes as a reference and plotted the difference for spectra with 5, 15, 30, and 50 modes. With only five modes for TE polarization 2D SHA gives quite accurate results, and the convergence was very uniform for all incident angles of the studied spectrum. The same plots for TM polarization are shown in Fig. 5, and they clearly show that the convergence for TM polarization is more complicated. Averages of the difference spectra for different numbers of modes are shown in Fig. 6. It is evident that 2D SHA simulations converge faster for TE polarization than for TM polarization. Since the tolerance of experimental measurements is typically around 1%, using five modes for TE polarization and 15 modes for TM polarization provides enough accuracy for the purpose of fitting experimental spectra. The higher number of

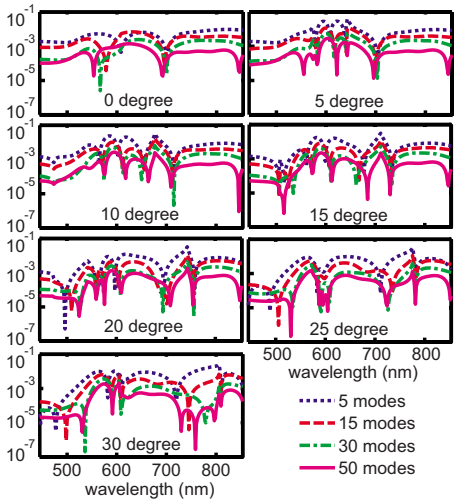

Fig. 5. (Color online) Convergence of 2D SHA for TM polarization. The difference spectra between 5, 15, 30, and 50 Fourier modes and the reference are plotted. The reference spectra are simulated using 2D SHA with 100 modes.

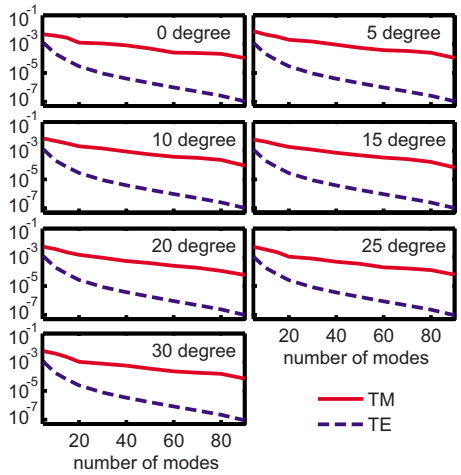

Fig. 6. (Color online) Average difference versus number of modes. The reference spectra are simulated using 2D SHA with 100 modes. For each number of modes the difference is averaged over the spectrum.

modes required for TM polarization is due to the resonance in TM polarization. At resonance, the fields near the gratings are strong and highly localized; therefore more modes are needed to resolve these fields. This is true for all incident angles.

5. SUMMARY

A nanofabricated subwavelength gold grating is utilized to validate our custom 2D SHA solver. The transmittance spectra of the subwavelength grating are obtained first from optical experiment and then from numerical simulations, which are performed for both TE and TM polarizations under 0°–30° oblique incidence.

First, the initial adjustment of the geometry and material properties is performed for all incident angles over a broad spectral range to minimize the experiment-simulation discrepancies caused by fabrication imperfections and the differences in the optical response of nanostructured gold versus that in bulk. The adjustments of the geometrical parameters are taken within a typical range of tolerances pertinent to electron beam lithography. Structural parameters affecting the optical response of gold (grain size and surface roughness) are incorporated as adjustable loss factors in the Drude part of the Drude–Lorentz model of the gold permittivity. The loss factor characterizing the overall quality of nanostructured gold strips is also chosen within a typical range achieved in nanofabricated gold elements [21,23]. This feedback from experimental realization is a necessary step. Once the initial adjustment is performed, an excellent agreement is achievable for all incident angles. We note that remaining minor discrepancies caused by stochastic disorder in otherwise periodic strips cannot be directly accounted for in our solver restricted to exactly periodic unit cells.

A separate effort is taken to estimate the convergence of the solver for different polarizations. As expected, the solver converges faster for TE polarization than for TM polarization, so for the purpose of fitting experimental data we usually need more modes for TM polarization, where multiple resonances are anticipated. For practical purposes 15 modes were enough to characterize the structure with accuracy better than that achievable in experiment.

A fully functional web-based tool with a graphical user interface and the 2D SHA solver based on the fast-converging numerical scheme is staged online and is now freely available to the academic and research community [19]; the solver can be used for characterization and homogenization of optical metamaterials under oblique light incidence [24,25].

APPENDIX A

The incident wave is a unit-amplitude monochromatic plane wave with a vacuum wavelength λ and an incident angle θ (Fig. 1). The vacuum wave vector is $k=2\pi/\lambda$. The incident plane is parallel to the x-y plane, and the polarization of the incident light is either TE, where the electric field is normal to the incident plane, or TM where the magnetic field is normal to the incident plane. For TE polarization the incident electric field can be expressed as $\mathbf{E}_i(\mathbf{r})=\hat{\mathbf{z}}E_{iz}\exp[i(\mathbf{k}_0\cdot\mathbf{r}-\omega t)]$, where $\mathbf{k}_0=\hat{\mathbf{x}}\alpha_0+\hat{\mathbf{y}}\beta_0$ is the incident wave vector with $\alpha_0=n_1k\cos\theta$, $\beta_0=n_1k\sin\theta$. For TM polarization the incident magnetic field can be expressed as $\mathbf{H}_i(\mathbf{r})=\hat{\mathbf{z}}H_{iz}\exp[i(\mathbf{k}_0\cdot\mathbf{r}-\omega t)]$.

For TE polarization only E_z, H_x, and H_y are nonzero. Then in each layer Maxwell's equations can be written as

$$\partial_y E_z = i\omega\mu_0 H_x,$$

$$-\partial_x E_z = i\omega\mu_0 H_y,$$

$$\partial_x H_y - \partial_y H_x = -i\omega\varepsilon E_z, \tag{A1}$$

where $\partial/\partial x=\partial_x$, $\partial/\partial y=\partial_y$, $\partial/\partial z=\partial_z$. Eliminate H_x and H_y, and we have the following equation for E_z:

$$\frac{\partial^2 E_z}{\partial x^2}+\frac{\partial^2 E_z}{\partial y^2}+\varepsilon_r k^2 E_z = 0. \tag{A2}$$

Because of the periodicity, E_z can be decomposed as $E_z(x,y)=\Sigma_{m,n}E_{zmn}\exp[i(k_{xm}x+k_{yn}y)]$, where m and n are integers ranging from $-\infty$ to ∞, and $k_{yn}=\beta_0+2\pi n/d$. k_{xm} is to be determined. The relative permittivity can be decomposed into Fourier series: $\varepsilon_r(y)=\varepsilon(y)/\varepsilon_0=\Sigma_q\varepsilon_q\exp[i2\pi qy/d]$. Substituting the expansions of fields and permittivity into Eq. (A2), and matching the coefficients of the term $\exp[i(k_{xm}x+k_{yn}y)]$ on both sides of the equation for each particular set of m and n, Maxwell's equation then becomes

$$E_{zmn}(\tilde{k}_{xm}^2+\tilde{k}_{yn}^2)=\sum_q \varepsilon_{n-q}E_{zmq}, \tag{A3}$$

where $\tilde{k}_{xm}=k_{xm}/k$ and $\tilde{k}_{yn}=k_{yn}/k$ are normalized wave vectors. Equation (A3) can be written in a matrix form for a fixed m:

$$\tilde{k}_{xm}^2\mathbf{E}_m=(\varepsilon-\tilde{\mathbf{k}}_y^2)\mathbf{E}_m, \tag{A4}$$

where $\tilde{\mathbf{k}}_y=[\tilde{k}_{yn}]$ is a diagonal matrix, $\mathbf{E}_m=[E_{zmn}]$ is a column vector, and ε is composed of Fourier coefficients ε_q:

$$\varepsilon = \begin{bmatrix} \varepsilon_0 & \varepsilon_{-1} & \varepsilon_{-2} & \cdots & \varepsilon_{-2M} \\ \varepsilon_1 & \varepsilon_0 & \varepsilon_{-1} & \cdots & \varepsilon_{-2M+1} \\ \vdots & \vdots & \vdots & \vdots & \vdots \\ \varepsilon_{2M} & \varepsilon_{2M-1} & \cdots & \varepsilon_1 & \varepsilon_0 \end{bmatrix}. \tag{A5}$$

Equation (A4) is a second-order eigenvalue equation with $\tilde{k}_{xm}^2$ being the eigenvalue and $\mathbf{E}_m$ being the eigenvector.

For TM polarization Maxwell's equations are

$$\partial_y H_z = -i\omega\varepsilon E_x,$$

$$\varepsilon^{-1}\partial_x H_z = i\omega E_y,$$

$$\partial_x E_y - \partial_y E_x = i\omega\mu_0 H_z. \tag{A6}$$

Note that the position of ε in Eq. (A6) is important: we must place ε on the right side of the first equation and $1/\varepsilon$ on the left side of the second equation to achieve fast convergence [8]. Using similar expansions, Eq. (A6) can be written in a matrix form:

$$-\omega\varepsilon_0\varepsilon\mathbf{E_{xm}} = k\tilde{\mathbf{k}}_y\mathbf{H_{zm}},$$

$$\omega\varepsilon_0\mathbf{E_{ym}} = k\tilde{k}_{xm}\bar{\varepsilon}\mathbf{H_{zm}},$$

$$k\tilde{k}_{xm}\mathbf{E_{ym}} - k\tilde{\mathbf{k}}_y\mathbf{E_{xm}} = \omega\mu_0\mathbf{H_{zm}}, \tag{A7}$$

where $\mathbf{E_{xm}}$, $\mathbf{E_{ym}}$, and $\mathbf{H_{zm}}$ are column vectors, and $\bar{\varepsilon}$ is formed by Fourier coefficients of $1/\varepsilon$:

$$\bar{\varepsilon} = \begin{bmatrix} (1/\varepsilon)_0 & (1/\varepsilon)_{-1} & (1/\varepsilon)_{-2} & \cdots & (1/\varepsilon)_{-2M} \\ (1/\varepsilon)_1 & (1/\varepsilon)_0 & (1/\varepsilon)_{-1} & \cdots & (1/\varepsilon)_{-2M+1} \\ \vdots & \vdots & \vdots & \vdots & \vdots \\ (1/\varepsilon)_{2M} & (1/\varepsilon)_{2M-1} & \cdots & (1/\varepsilon)_1 & (1/\varepsilon)_0 \end{bmatrix}. \tag{A8}$$

Eliminating $\mathbf{E_{xm}}$ and $\mathbf{E_{ym}}$ from Eq. (A7), we obtain the eigenvalue equation for TM polarization:

$$\tilde{k}_{xm}^2\bar{\varepsilon}\mathbf{H_{zm}} = (\mathbf{I} - \tilde{\mathbf{k}}_y\varepsilon^{-1}\tilde{\mathbf{k}}_y)\mathbf{H_{zm}}. \tag{A9}$$

This is a second-order generalized eigenvalue problem with $\tilde{k}_{xm}^2$ being the eigenvalue and $\mathbf{H_{zm}}$ being the eigenvector. It can be solved as a standard eigenvalue problem:

$$\tilde{k}_{xm}^2\mathbf{H_{zm}} = \bar{\varepsilon}^{-1}(\mathbf{I} - \tilde{\mathbf{k}}_y\varepsilon^{-1}\tilde{\mathbf{k}}_y)\mathbf{H_{zm}}. \tag{A10}$$

The dimensions of the matrix equations (A4) and (A10) are infinite; however in practical implementations the matrices have to be truncated.

The eigenvectors obtained from Eqs. (A4) and (A10) are not unique as they can be scaled by arbitrary constants; therefore boundary conditions are used to uniquely determine the system under study. In our study we use the *S*-matrix method proposed in [9] to match the tangential electric and magnetic fields for multilayer gratings. In the pth layer each eigenvalue Λ_m corresponds to two wave vectors: $\tilde{k}_{xm} = \pm\sqrt{\Lambda_m}$; hence two sets of coefficients, $\mathbf{u}^{(p)}$ and $\mathbf{d}^{(p)}$ for upward and downward propagating waves, respectively, need to be determined. Here $\mathbf{u}^{(p)}$ and $\mathbf{d}^{(p)}$ are defined at the lower bound of the pth layer. Using the same notation as in [9] (Fig. 1), the boundary conditions can be written as

$$\begin{bmatrix} \mathbf{u}^{(p+1)} \\ \mathbf{d}^{(0)} \end{bmatrix} = \begin{bmatrix} \mathbf{T}_{uu}^{(p)} & \mathbf{R}_{ud}^{(p)} \\ \mathbf{R}_{du}^{(p)} & \mathbf{T}_{dd}^{(p)} \end{bmatrix} \begin{bmatrix} \mathbf{u}^{(0)} \\ \mathbf{d}^{(p+1)} \end{bmatrix}, \tag{A11}$$

where $\mathbf{T}_{uu}^{(p)}$ and $\mathbf{T}_{dd}^{(p)}$ are two transmission transfer matrices, and $\mathbf{R}_{ud}^{(p)}$ and $\mathbf{R}_{du}^{(p)}$ are two reflection transfer matrices. We assume that the incident light comes only from the top, then $\mathbf{u}^{(0)}=0$, and only $\mathbf{T}_{dd}^{(p)}$ and $\mathbf{R}_{ud}^{(p)}$ are of interest. This is called half-matrix recursion in [10], and the transmission and reflection matrices can be obtained recursively by the following steps. First we calculate $\mathbf{Q}_E^{(p)}$ and $\mathbf{Q}_H^{(p)}$:

$$\mathbf{Q}_E^{(p)} = (\mathbf{E}^{(p+1)})^{-1}\mathbf{E}^{(p)},$$

$$\mathbf{Q}_H^{(p)} = (\mathbf{H}^{(p+1)})^{-1}\mathbf{H}^{(p)}, \tag{A12}$$

where for TE polarization $\mathbf{E}^{(p)}=\mathbf{E}_z^{(p)}$ is the eigenvector matrix, and $\mathbf{H}^{(p)}=\mathbf{H}_y^{(p)}=-\mathbf{E}_z^{(p)}\tilde{\mathbf{k}}_x^{(p)}$, where $\tilde{\mathbf{k}}_x^{(p)}$ is a diagonal matrix with the diagonal elements $\tilde{k}_{xm}$; and for TM polarization $\mathbf{H}^{(p)}=\mathbf{H}_z^{(p)}$ is the eigenvector matrix, and $\mathbf{E}^{(p)}=\mathbf{E}_y^{(p)}=\bar{\varepsilon}^{(p)}\mathbf{H}_z^{(p)}\tilde{\mathbf{k}}_x^{(p)}$. If a layer is homogeneous, then we have $\tilde{k}_{xn}=\sqrt{\varepsilon_r-\tilde{k}_{yn}^2}$, and for TE polarization the matrices are $\mathbf{E}_z=\mathbf{I}$, $\mathbf{H}_y=-\tilde{\mathbf{k}}_x$; for TM polarization the matrices are $\mathbf{H}_z=\mathbf{I}$, $\mathbf{E}_y=\tilde{\mathbf{k}}_x/\varepsilon_r$. To make the recursion stable, the imaginary part of $\tilde{k}_{xm}$ should be positive so that the fields are always decaying. Then we define

$$\mathbf{t}_1^{(p)} = (\mathbf{Q}_E^{(p)} + \mathbf{Q}_H^{(p)})/2,$$

$$\mathbf{t}_2^{(p)} = (\mathbf{Q}_E^{(p)} - \mathbf{Q}_H^{(p)})/2 \quad \text{for TE},$$

$$\text{or } \mathbf{t}_2^{(p)} = (\mathbf{Q}_H^{(p)} - \mathbf{Q}_E^{(p)})/2 \quad \text{for TM},$$

$$\Omega^{(p)} = \Phi^{(p)}\mathbf{R}_{ud}^{(p-1)}\Phi^{(p)}, \tag{A13}$$

where $\Phi^{(p)}=[\exp(ik_{xm}^{(p)}h_p)]$ is a diagonal matrix. Finally $\mathbf{T}_{dd}^{(p)}$ and $\mathbf{R}_{ud}^{(p)}$ are calculated as

$$\mathbf{R}_{ud}^{(p)} = [\mathbf{t}_2^{(p)} + \mathbf{t}_1^{(p)}\Omega^{(p)}][\mathbf{t}_1^{(p)} + \mathbf{t}_2^{(p)}\Omega^{(p)}]^{-1},$$

$$\mathbf{T}_{dd}^{(p)} = \mathbf{T}_{dd}^{(p-1)}\Phi^{(p)}[\mathbf{t}_1^{(p)} + \mathbf{t}_2^{(p)}\Omega^{(p)}]^{-1}. \tag{A14}$$

For the first iteration, we can use a virtual layer (the zeroth layer) with zero thickness below the first interface (the layer between the interfaces $p=0$ and $p=-1$). Then the initial values are $\mathbf{T}_{dd}^{(-1)}=\mathbf{I}$, $\mathbf{R}_{ud}^{(-1)}=0$, $\Phi^{(0)}=\mathbf{I}$, and $\Omega^{(0)}=0$; hence $\mathbf{T}_{dd}^{(0)}=(\mathbf{t}_1^{(0)})^{-1}$ and $\mathbf{R}_{ud}^{(p)}=\mathbf{t}_2^{(0)}\mathbf{T}_{dd}^{(0)}$. For TE polarization we use $\mathbf{E}^{(0)}=\mathbf{I}$ and $\mathbf{H}^{(0)}=-\tilde{\mathbf{k}}_x$, and for TM polarization $\mathbf{H}^{(0)}=\mathbf{I}$ and $\mathbf{E}^{(0)}=\tilde{\mathbf{k}}_x/n_2^2$. Since the incident wave is a plane wave the input then is defined as

$$\mathbf{d}^{(N+1)} = \Big[\underbrace{0 \ \cdots \ 0}_{M} \ 1 \ \underbrace{0 \ \cdots \ 0}_{M}\Big]^T,$$

where M is the truncation order, the transmitted fields

are calculated by $\mathbf{d}^{(0)}=\mathbf{T}_{dd}^{(N)}\mathbf{d}^{(N+1)}$, and the reflected fields are calculated by $\mathbf{u}^{(N+1)}=\mathbf{R}_{ud}^{(N)}\mathbf{d}^{(N+1)}$. Note that for TE polarization the coefficients are for the E-field, and for TM polarization the coefficients are for the H-field.

ACKNOWLEDGMENT

The authors thank Joshua D. Borneman for providing necessary material properties.

REFERENCES

1. C. B. Burckhardt, "Diffraction of a plane wave at a sinusoidally stratified dielectric grating," J. Opt. Soc. Am. **56**, 1502–1509 (1966).
2. F. G. Kaspar, "Diffraction by thick, periodically stratified gratings with complex dielectric-constant," J. Opt. Soc. Am. **63**, 37–45 (1973).
3. K. Knop, "Rigorous diffraction theory for transmission phase gratings with deep rectangular grooves," J. Opt. Soc. Am. **68**, 1206–1210 (1978).
4. M. G. Moharam and T. K. Gaylord, "Rigorous coupled-wave analysis of planar-grating diffraction," J. Opt. Soc. Am. **71**, 811–818 (1981).
5. M. G. Moharam and T. K. Gaylord, "Rigorous coupled-wave analysis of grating diffraction-E-mode polarization and losses," J. Opt. Soc. Am. **73**, 451–455 (1983).
6. P. Lalanne and G. M. Morris, "Highly improved convergence of the coupled-wave method for TM polarization," J. Opt. Soc. Am. A **13**, 779–784 (1996).
7. G. Granet and B. Guizal, "Efficient implementation of the coupled-wave method for metallic lamellar gratings in TM polarization," J. Opt. Soc. Am. A **13**, 1019–1023 (1996).
8. L. F. Li, "Use of Fourier series in the analysis of discontinuous periodic structures," J. Opt. Soc. Am. A **13**, 1870–1876 (1996).
9. L. F. Li, "Formulation and comparison of two recursive matrix algorithms for modeling layered diffraction gratings," J. Opt. Soc. Am. A **13**, 1024–1035 (1996).
10. L. F. Li, "Note on the S-matrix propagation algorithm," J. Opt. Soc. Am. A **20**, 655–660 (2003).
11. J. B. Pendry, "Negative refraction makes a perfect lens," Phys. Rev. Lett. **85**, 3966–3969 (2000).
12. W. S. Cai, U. K. Chettiar, H. K. Yuan, V. C. de Silva, A. V. Kildishev, V. P. Drachev, and V. M. Shalaev, "Metamagnetics with rainbow colors," Opt. Express **15**, 3333–3341 (2007).
13. U. K. Chettiar, A. V. Kildishev, T. A. Klar, and V. M. Shalaev, "Negative index metamaterial combining magnetic resonators with metal films," Opt. Express **14**, 7872–7877 (2006).
14. V. P. Drachev, W. Cai, U. Chettiar, H. K. Yuan, A. K. Sarychev, A. V. Kildishev, G. Klimeck, and V. M. Shalaev, "Experimental verification of an optical negative-index material," Laser Phys. Lett. **3**, 49–55 (2006).
15. V. M. Shalaev, W. S. Cai, U. K. Chettiar, H. K. Yuan, A. K. Sarychev, V. P. Drachev, and A. V. Kildishev, "Negative index of refraction in optical metamaterials," Opt. Lett. **30**, 3356–3358 (2005).
16. H. K. Yuan, U. K. Chettiar, W. S. Cai, A. V. Kildishev, A. Boltasseva, V. P. Drachev, and V. M. Shalaev, "A negative permeability material at red light," Opt. Express **15**, 1076–1083 (2007).
17. S. Zhang, W. J. Fan, N. C. Panoiu, K. J. Malloy, R. M. Osgood, and S. R. J. Brueck, "Experimental demonstration of near-infrared negative-index metamaterials," Phys. Rev. Lett. **95**, 137404 (2005).
18. A. V. Kildishev and U. K. Chettiar, "Cascading optical negative index metamaterials," Appl. Comput. Electromagn. Soc. J. **22**, 172–183 (2007).
19. X. Ni, Z. Liu, F. Gu, M. G. Pacheco, A. V. Kildishev, and J. Borneman, "PhotonicsSHA-2D: Modeling of single-period multilayer optical gratings and metamaterials," (2009), DOI 10254/nanohub-r6977.9.
20. P. B. Johnson and R. W. Christy, "Optical constants of noble metals," Phys. Rev. B **6**, 4370–4379 (1972).
21. V. P. Drachev, U. K. Chettiar, A. V. Kildishev, H. K. Yuan, W. S. Cai, and V. M. Shalaev, "The Ag dielectric function in plasmonic metamaterials," Opt. Express **16**, 1186–1195 (2008).
22. E. G. Loewen and E. Popov, *Diffraction Gratings and Applications* (Marcel Dekker, 1997).
23. K.-P. Chen, V. P. Drachev, J. D. Borneman, A. V. Kildishev, and V. M. Shalaev, "Drude relaxation rate in grained gold nanoantennas," Nano Lett. **10**, 916–922 (2010), DOI 10.1021/nl9037246.
24. K. B. Alici and E. Ozbay, "Oblique response of a split-ring-resonator-based left-handed metamaterial slab," Opt. Lett. **34**, 2294–2296 (2009).
25. C. Menzel, C. Helgert, J. Upping, C. Rockstuhl, E. B. Kley, R. B. Wehrspohn, T. Pertsch, and F. Lederer, "Angular resolved effective optical properties of a Swiss cross metamaterial," Appl. Phys. Lett. **95** (2009).